CMB and Lyman-α Constraints on Dark Matter Decays to Photons

Francesco Capozzi,[1,2] Ricardo Z. Ferreira,[3] Laura Lopez-Honorez,[4,5] and Olga Mena[6]

[1]*Dipartimento di Scienze Fisiche e Chimiche, Universita degli Studi dell'Aquila, 67100 L'Aquila, Italy*

[2]*Istituto Nazionale di Fisica Nucleare (INFN), Laboratori Nazionali del Gran Sasso, 67100 Assergi (AQ), Italy*

[3]*Institut de F?sica d'Altes Energies (IFAE) and Barcelona Institute of Science and Technology (BIST), Campus UAB, 08193 Bellaterra, Barcelona, Spain*

[4]*Service de Physique Theorique, Universite Libre de Bruxelles, C.P. 225, B-1050 Brussels, Belgium*

[5]*Theoretische Natuurkunde & The International Solvay Institutes, Vrije Universiteit Brussel, Pleinlaan 2, B-1050 Brussels, Belgium*

[6]*Instituto de Física Corpuscular (IFIC), University of Valencia-CSIC, Parc Científic UV, c/ Catedrático José Beltrán 2, E-46980 Paterna, Spain*

Abstract

We improve the CMB bounds on sub-keV dark matter and extend previous bounds from Lyman-α observations to the same mass range, resulting in new and competitive constraints on axion-like particles (ALPs) decaying into two photons.

Keywords: dark matter, axion-like particles, dark matter decay, reionization, Lyman-α
DOI: 10.31526/BSM-2023.6

1. INTRODUCTION

In this work, we revisit the imprints on the ionization history, from the recombination period until present times, and on the IGM temperature, at low redshifts ($z \lesssim 6$), for DM decays into two photons. We exploit Planck 2018 data to update previous CMB constraints on the 20.4 eV to keV mass range, and Lyman-α data to extend previous analyses for heavier DM masses to the same mass window, in which a plethora of axion-like particle (ALPs) DM models may lie. The lower end of the mass range corresponds to twice the energy necessary for a Lyman-α transition in the Hydrogen atom. At the upper end, strong constraints from X-ray searches [1] dramatically prevent us to improve over the existing bounds with CMB and Lyman-α data.

For the CMB constraints, we will consider Planck 2018 data and extend the work of [1, 2] in a few ways. First, we take into account the energy injection efficiencies by making use of the `DarkHistory` code [3] and investigating the impact on the bounds of multiple reionization scenarios. We consider two well-motivated astrophysical models for the galactic UV/X-ray background [4, 5] and self-consistently take into account the DM feedback on the IGM temperature and on the ionization fractions by means of the use of `DarkHistory`. We then perform a full MCMC analysis in which we vary not only the relevant DM parameters but also other fiducial cosmological parameters. On the other hand, we show that CMB bounds are expected to become competitive to those of Leo-T with future CMB surveys, independently of the assumed reionization history.

Concerning the Lyman-α data analysis, we shall derive new bounds by extending the analysis provided in [6] to lower DM masses. We will follow the conservative approach proposed in [6], where robust constraints on DM from the IGM temperature were derived by fixing the reionization history to the Planck fiducial model and by neglecting the photoheating from astrophysical sources thus overcoming the large uncertainties associated to the astrophysical scenarios.

2. IONIZED FRACTION AND IGM TEMPERATURE EVOLUTION

The evolution of the different ionization fractions is entangled with the evolution of the IGM temperature. The system of equations that keeps track of T_m and of the different contributions to x_e reads [7, 8]:

$$\dot{Y} = \dot{Y}^{(0)} + \dot{Y}^{\rm DM} + \dot{Y}^{\rm astro}, \quad \text{where } Y = \begin{pmatrix} T_m \\ x_{\rm HII} \\ x_{\rm HeII} \\ x_{\rm HeIII} \end{pmatrix}, \tag{1}$$

where the ionized fractions x_X correspond to the ratios $x_X = n_X/n_{\rm H}$ where n_H is the total Hydrogen density and $X =$ HII, HeII, and HeIII stands for Hydrogen, singly ionized Helium and doubly ionized Helium, respectively. The contributions to the evolution of the temperature and ionized fractions are divided into three different terms. The first term $\dot{Y}^{(0)}$ accounts for adiabatic evolution, Compton scatterings and atomic processes, while the $\dot{Y}^{\rm DM}$ term is driven by DM energy injection in the medium. The third term $\dot{Y}^{\rm astro}$ is particularly relevant at low redshifts when astrophysics sources provide an extra source of photoionization and photoheating, triggering reionization.

2.1. Adiabatic Cooling, Compton Scattering and Atomic Processes

The contribution to the IGM temperature evolution reads [3, 6]:

$$\dot{T}_m^{(0)} = -2HT_m + \Gamma_C \left(T_{\rm CMB} - T_m\right) + \dot{T}_m^{\rm atom}. \tag{2}$$

The first term accounts for adiabatic cooling whereas the second term describes Compton heating/cooling with Γ_C the Compton scattering rate, $T_{\rm CMB}$ the CMB temperature, and H is the Hubble rate. The last term includes multiple heating/cooling contributions due to atomic processes (recombination, collisional ionization, collisional excitation and bremsstrahlung) whose rates are given in [9, 10] (see also [6]). On the other hand, the evolutions of the ionized fractions is governed by

$$\dot{x}_X^{(0)} = \dot{x}_X^{\rm ion} - \dot{x}_X^{\rm rec}, \tag{3}$$

where $x_X^{\rm ion}$ ($x_X^{\rm rec}$) accounts for ionization (recombination) processes.

2.2. Dark Matter Energy Injection and Deposition

The $\dot{Y}^{\rm DM}$ term of equation (1) accounts for the dark matter annihilation/decay contributions. To describe this term, let us focus on an ALP dark matter particle a of mass m_a that decays into two photons of energy $m_a/2$ at a rate $\Gamma_{\rm dec} \gg t_0^{-1}$ (where t_0 is the age of the universe). The energy injected per unit of time and volume is given by

$$\left(\frac{dE(z)}{dt\,dV}\right)_{\rm injected} = \rho_a (1+z)^3 \Gamma_{\rm dec}, \tag{4}$$

where ρ_a is the energy density of the DM particle today and the decay rate is parametrized as

$$\Gamma_{\rm dec} = g_{a\gamma\gamma}^2 m_a^3/(64\pi), \tag{5}$$

with $g_{a\gamma\gamma}$ the ALP-photon coupling. In the next sections, we will phrase our constraints on DM decays to photons in terms of the ALPs parameters m_a and $g_{a\gamma\gamma}$. Note however that, by properly re-expressing the bounds on $g_{a\gamma\gamma}$ in terms of the DM lifetime $\Gamma_{\rm dec}^{-1}$, our constraints apply to any DM model decaying to two photons.

The injected energy may not be deposited instantaneously into the medium due to the cooling of primary particles. In addition, there are multiple channels c of energy deposition including IGM heating (denoted with $c =$ heat), Hydrogen ionization ($c =$ HII), Helium single or double ionization ($c =$ HeII or HeIII), and neutral atom excitation ($c =$ exc). The fraction of energy injected that is deposited in the different channels can be expressed as [11]

$$\left(\frac{dE_c\left(x_e, z\right)}{dt\,dV}\right)_{\rm deposited} = f_c\left(x_e, z\right) \left(\frac{dE(z)}{dt\,dV}\right)_{\rm injected}, \tag{6}$$

where the coefficients, $f_c(x_e, z)$, are the DM energy deposition efficiencies. They account for all the details associated to the delay in energy deposition and separation into different channels c at a given redshift z and free electron fraction x_e (that is a function of the different ionization fractions x_X). We make use of `DarkHistory` [3] to obtain the $f_c(x_e, z)$ functions. In the `DarkHistory` code, the term $\dot{Y}^{\rm DM}$ in equation (1) takes the form:

$$\dot{Y}^{\rm DM} = A \times \frac{1}{n_{\rm H}} \left(\frac{dE(z)}{dt\,dV}\right)_{\rm injected}, \tag{7}$$

where the prefactor $A = A(f_c(x_e, z))$ is a function of the deposition fractions $f_c(x_e, z)$.

2.3. Reionization

A useful quantity when comparing different reionization histories is the optical depth to reionization, τ, that we define as

$$\tau = \int_0^{z_{e,\rm min}} dz\, n_e \sigma_T \frac{dt}{dz}, \tag{8}$$

i.e., the integral, between today and the time at which the electron fraction displays a minimum (tagged as $z_{e,\rm min}$), of the free electron number density, $n_e(z)$, multiplied by the Thompson cross-section, σ_T. This is the prescription followed in the publicly available `CLASS` Boltzmann solver code [12, 13, 14].

2.3.1. The Hyperbolic Tangent Function

The most widely used model for the reionization history exploits the hyperbolic tangent function [15]:

$$x_e^{\tanh}(z) = \frac{1+\mathcal{F}_{\rm He}}{2}\left(1+\tanh\left[\frac{y(z_{\rm reio})-y(z)}{\Delta_y}\right]\right), \tag{9}$$

where $\mathcal{F}_{\rm He} = n_{\rm HeII}/n_{\rm H}$ is the ratio of singly ionized Helium to Hydrogen atoms, $y(z) = (1+z)^\gamma$, $\Delta_y = \gamma(1+z_{\rm reio})^{\gamma-1}\Delta_z$, where Δ_z is the width of the transition. The parameters Δ_z and γ are the are fixed to 0.5 and 3/2, respectively. The only free parameter that we will vary here is the reionization redshift $z_{\rm reio}$. With such a reionization model, Planck 2018 temperature and polarization data gives rise to an optical depth to reionization

$$\tau_{\rm Pl} = 0.054 \quad \text{with } \sigma_{\rm Pl}(\tau) = 0.007, \tag{10}$$

where $\sigma_{\rm Pl}(\tau)$ denotes the 68% CL error [16]. This implies a mid-point redshift of reionization $z_{\rm reio} = 7.68 \pm 0.79$ at 68% CL, suggesting that the Universe was fully reionized by $z \simeq 6$. The interest in this model is justified by the fact that it is easy to explore a large set of reionization histories by varying $z_{\rm reio}$ or even the reionization width. In the left panel of Figure 1, the continuous curves illustrate the ionized fraction evolution within an hyperbolic tangent model assuming $z_{\rm reio} = 7.68$. The blue curve assumes a negligible energy injection from DM decays and is in agreement with Planck 2018 data. The yellow curve is obtained with a larger coupling to photons affecting the ionization history at $z \gtrsim z_{\rm reio}$.

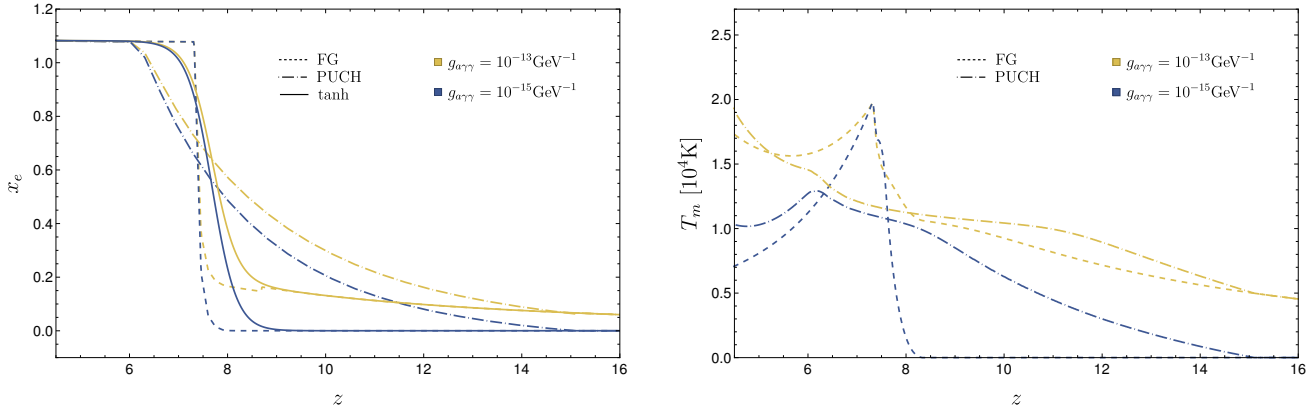

FIGURE 1: *Ionisation and IGM temperature histories* for different reionization models including the energy injections from the decays into two photons of a DM particle of mass $m_a = 95\,\text{eV}$ and two different couplings to photons. On the left panel, we focus on the free electron fraction illustrating with blue and orange curves the reionization models of FG (dashed lines), PUCH (dot-dashed lines) and hyperbolic tangent (solid lines) for $z_{\rm reio} = 7.68$ (continuous) and consider DM energy injection for two possible values of the DM-photon coupling $g_{a\gamma\gamma}$: 10^{-15} and $10^{-13}\,\text{GeV}^{-1}$. The right panel depicts the matter temperature evolution in redshift for the very same two astrophysical-based reionization models and couplings $g_{a\gamma\gamma}$.

2.3.2. Reionization from Stars

Apart from the hyperbolic tangent model, in this paper, we shall also consider two explicit reionization models from Puchwein et al. [5] and Fauchere-Giguère [4], that we denote by PUCH and FG, respectively, for short. Those reionization scenarios rely on observations of the UV and X-ray background emission from galaxies to model the photoionization ($\Gamma_{\rm X}^{\gamma\text{-ion}}$) and photoheating ($\mathcal{H}_{\rm X}^{\gamma\text{-heat}}$) rates from astrophysical sources contributing to the $\dot{Y}^{\rm astro}$ term of equation (1) as [3, 6]

$$\begin{pmatrix} \dot{T}_m^{\rm astro} \\ \dot{x}_{\rm X}^{\rm astro} \end{pmatrix} = \begin{pmatrix} \frac{2}{3(1+\mathcal{F}_{\rm He}+x_e)n_{\rm H}} \sum_{\rm X} \mathcal{H}_{\rm X}^{\gamma\text{-heat}} \\ x_{\rm X}\Gamma_{\rm X}^{\gamma\text{-ion}} \end{pmatrix}, \tag{11}$$

where X={HII, HeII, HeIII}.

There are several differences between the PUCH and FG models. First, the onset of reionization, $z_{\rm A}^{\rm max}$, is given by $z_{\rm PUCH}^{\rm max} = 15.1$ and $z_{\rm FG}^{\rm max} = 7.8$ for the PUCH and FG reionization models, respectively. Moreover, in the FG model reionization is relatively rapid compared to the PUCH model. These differences are illustrated in Figure 1, where we depict the redshift evolution of x_e (left panel) and T_m (right panel) with a dashed line for the FG model and a dot-dashed line for the PUCH model. Let us emphasize that, for redshifts above $z_{\rm A}^{\rm max}$ and fixed values of the coupling to photons, all $x_e(z)$ and $T_m(z)$ curves are identical by construction. Indeed, the $\dot{Y}^{\rm astro}$ term only accounts for extra energy injection from stars at $z < z_A^{\rm max}$.

In the left panel of Figure 1, where we show the evolution of the free electron fraction as a function of the redshift, we consider a DM particle with 95 eV mass and two distinct couplings to photons (see equation (5)), $g_{a\gamma\gamma} = 10^{-15}\,\text{GeV}^{-1}$ (blue lines) and

$g_{a\gamma\gamma} = 10^{-13}\,\mathrm{GeV}^{-1}$ (orange lines), that correspond, respectively, to a negligible and a significant DM energy injection. After implementing the PUCH and FG models in `DarkHistory` and using equation (8) to evaluate the optical depth, we obtain for the default PUCH and FG reionization models (i.e., the blue curves with negligible DM energy injection):

$$\tau_{\mathrm{PUCH}} = 0.064, \quad \tau_{\mathrm{FG}} = 0.052. \tag{12}$$

Comparing these optical depths to the one reported by Planck in equation (10), it is clear that the FG reionization model will lead to more conservative bounds on the DM scenario than the PUCH model. Indeed, the latter gives rise to a larger optical depth to reionization leaving less room for an extra DM contribution to the free electron fraction.

The IGM temperature evolution is depicted in the right panel of Figure 1. We show in blue (orange) an ALP-photon coupling of $g_{a\gamma\gamma} = 10^{-15}\,\mathrm{GeV}^{-1}$ ($g_{a\gamma\gamma} = 10^{-13}\,\mathrm{GeV}^{-1}$) and the dashed and dot-dashed curves show the IGM temperature evolution in the PUCH and FG models. We clearly see the differences between these two reionization models as well as the impact of DM energy injection. In all cases, the DM decay into photons induces higher IGM temperature for larger couplings to photons (well visible for $z > z^{\mathrm{max}}_{\mathrm{PUCH}}$). Also, for both PUCH and FG models, we see the presence of a bump in the IGM temperature that roughly starts at the onset of reionization and peaks when the latter is completed. In the PUCH model, the changes in the IGM temperature are smoother as reionization starts at higher redshifts than in the FG case. In the FG model, reionization happens on a much shorter time scale, the changes are more abrupt and cause a sharper peak in the evolution of the matter temperature at reionization ($z \simeq 8$). Notice though that the values of T_m on this peak of temperature remain at most within a factor $\sim$2 from the values of T_m in the $z < 6$ redshift range, where current observations of the IGM temperature are relevant.

3. CMB ANALYSIS

3.1. Energy Deposition from DM $\to \gamma\gamma$ *in* `CLASS`

The `CLASS` Boltzmann solver [17, 13] can account for exotic energy injection at high redshifts ($z \gtrsim z_{\mathrm{reio}}$) building upon the `ExoCLASS` extension, see [18, 19]. In the case of DM decays, the default implementation in the `injection` module fixes the energy deposition efficiencies $f_c(x_e, z)$ to those given in [20], which essentially reduce to $f_c(x_e, z) = 1/3$ for $c =$ HII, heat and exc at large z. At $z \lesssim z_{\mathrm{reio}}$ the ionized fraction follows by default the hyperbolic tangent model presented in Section 2.3.1. The `thermodynamics` module allows however to implement any reionization history by providing a list of $x_e(z)$ points between which `CLASS` interpolates.

In order to efficiently account for a more accurate treatment of energy deposition from dark matter and stars, we have made slight modifications of both the `injection` and `thermodynamics` modules of `CLASS`:

(i) At $z \lesssim z^{\mathrm{max}}_{\mathrm{A}}$, we account for specific reionization from stars (PUCH or FG models) interpolating, within the `thermodynamics` module, a tabulated evolution of $x_e(z)$ between $z = 6$ and $z^{\mathrm{max}}_{\mathrm{A}}$ for different values of the DM parameters m_a and $g_{a\gamma\gamma}$ within the ranges of interest, see Section 3.2. These tabulated values have been obtained with `DarkHistory` and take into account the convoluted effect of DM decay and reionization from stars.

(ii) Before reionization, we have made use of an approximation to the energy deposition, described in equation (6), that facilitates the computation of energy injection efficiencies for any DM mass and couplings relevant here. We discuss the latter in more detail below. Let us also mention that in all cases we have made use of the default `HyRec` recombination algorithm [21, 22].

It is well known that in the case of dark matter decays, efficient energy deposition is delayed to later times with respect to, e.g., the annihilating DM case, see for example the discussion in [6, 23, 24, 25, 26]. In [26], it was shown by means of a principal component analysis that the impact of DM decays on the CMB (between reionization and recombination) is well captured using the energy deposition efficiencies $f_c(x_e, z)$ at redshift $z \simeq 300$, as expected from the results of [27]. This allows to shortcut the treatment of high redshift energy deposition by using:

$$\left(\frac{dE_c\,(x_e,z)}{dt\,dV}\right)_{\mathrm{deposited}} = f_c^{\mathrm{eff}} \left(\frac{dE\,(x_e,z)}{dt\,dV}\right)_{\mathrm{injected}} \qquad \text{for } z > z^{\mathrm{max}}_{\mathrm{A}}, \tag{13}$$

where $f_c^{\mathrm{eff}} = f_c(x_e, z = 300)$ is used as an effective energy deposition efficiency parameter. In our CMB analysis, we use this approximation at high redshifts instead of the full $f_c(x_e, z)$ treatment of equation (6). For $m_a \lesssim \mathcal{O}(100)$ eV, ionization becomes the main channel for energy deposition at large redshifts, except below $m_a < 26$ eV where the excitation channel is dominant.

In [26], it was explicitly checked that f_c^{eff} is in excellent agreement with the first principal component of $f_c(x_e, z)$ for decaying DM masses above 10^4 eV. Making use of the `DarkHistory` package and of our modified `CLASS` code, we found an excellent agreement on $x_e(z)$ when comparing the effective or the full energy deposition approaches for $z_{\mathrm{reio}} < z < 10^3$ and dark matter masses between 20.4 eV and 10^4 eV. This is illustrated in Figure 2 where we focus on a dark matter particle with a mass $m_a = 95$ eV decaying into two photons with a coupling $g_{a\gamma\gamma}$ between $10^{-13}\,\mathrm{GeV}^{-1}$ (orange lines) and $10^{-15}\,\mathrm{GeV}^{-1}$ (blue lines) and assuming a PUCH reionization model. The continuous colored lines are obtained with the `DarkHistory` software using the full treatment of $f_c(x_e, z)$, as in equation (6), while the dashed lines are obtained with the `CLASS` code, making use of the effective energy deposition of equation (13) with $f_c^{\mathrm{eff}} = f_c(x_e, z = 300)$ from `DarkHistory`. Notice that continuous and dashed lines are almost identical as expected.

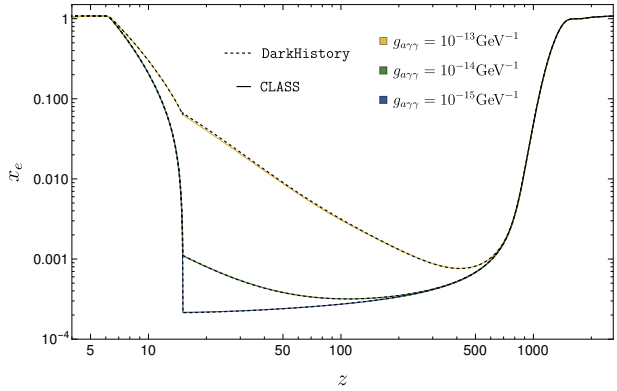

FIGURE 2: *Comparison of the different numerical approaches* when considering the dark matter energy injections through decays of a dark matter particle of mass $m_a = 95\,\text{eV}$ and different couplings and reionization models. On the left panel, we depict the ionization history when considering a PUCH reionization model in our modified version of the `CLASS` Boltzmann package code (dashed lines) and that recovered from the full treatment of the `DarkHistory` package (continuous colored lines) for couplings $g_{a\gamma\gamma} = 10^{-15}$ (in blue), 10^{-14} (in green) and $10^{-13}\,\text{GeV}^{-1}$ (in orange).

3.2. Current and Future Constraints for Different Reionization Models

Based on the prescription for energy injection at recombination and reionization described in Section 3.1, we now use Planck 2018 data to derive constraints on sub-keV decaying dark matter. We present the bounds in the plane of the DM mass m_a and DM coupling to photons $g_{a\gamma\gamma}$, that effectively set the decay rate (see equation (5)). We focus on the mass and coupling ranges:

$$m_a \supset \left[10, 10^4\right]\,\text{eV}, \quad \log_{10}\left[g_{a\gamma\gamma} \times \text{GeV}\right] \supset [-12, -16]. \tag{14}$$

We also analyse the impact of the underlying reionization model on the constraints. More precisely, we derive the bounds that arise in the case of the hyperbolic tangent reionization model of Section 2.3.1, denoted by tanh for short, and compare them to the explicit FG and PUCH astrophysical models presented in Section 2.3.2.

We can now perform a full Monte Carlo analysis. The minimal set of cosmological parameters considered in our analysis includes:

$$\left\{\Omega_b h^2, \Omega_a h^2, 100\theta_*, \ln\left[10^{10} A_s\right], n_s, \log_{10}\left[m_a/\text{eV}\right], \log_{10}\left[g_{a\gamma\gamma} \times \text{GeV}\right]\right\}. \tag{15}$$

In the case of the PUCH and FG reionization models, we work with fixed photoionization and photoheating rates and thus perform the MCMC on the set of parameters (see equation (15)). In contrast, in the case of the hyperbolic tangent model, the set of parameters is supplemented by the reionization redshift z_{reio}. In the latter case, we can thus effectively marginalize over multiple reionization scenarios. In equation (15), $\Omega_b h^2$ and $\Omega_a h^2$ are the relative baryon and decaying dark matter densities today, θ_* is the acoustic scale angle and A_s and n_s are, respectively, the amplitude and spectral index of the primordial power spectrum. For the latter purposes, we have run the `MontePython` software [29] interfaced with our modified version of `CLASS` and used the baseline TT, TE, EE + lowE Planck 2018 likelihoods. The resulting bounds at 99% CL are depicted in Figure 3 in thick red continuous, dashed and dot-dashed lines for, respectively, the tanh, FG and PUCH reionization models. Interestingly, we notice that the results of the Monte Carlo analysis are in good agreement with the estimated bounds (gray lines). In addition, we note that the tanh model, marginalizing over the reionization redshift in the range $z_{\text{reio}} = 5$ to 13, leads to a constraint on the parameter space that is very similar to the conservative case of a FG reionization scenario.

The CMB bounds derived here are more stringent than the previous ones from [1, 2]. Indeed, our analysis differs from the previous ones in a few aspects. First, we use a more recent CMB data release, which translates into a lower value of τ. Second, we make use of more accurate values for the energy deposition efficiency coefficients by including the $f_c(x_e, z = 300)$ computed from `DarkHistory` and we exploit the full CMB anisotropy spectrum information rather than just the optical depth to reionization. Also, we perform a full MCMC analysis to extract the constraints from CMB anisotropies. Let us also emphasize that our bounds are competitive with the constraints from the radiative cooling gas rate of the Leo-T dwarf galaxy [28] in the case of the more aggressive PUCH reionization scenario.

Concerning future prospects, CMB-S4 surveys are expected to reach a 1σ uncertainty on the optical depth to reionization of $\sigma(\tau) = 0.0025$ [30]. Preliminary estimates also show that by combining measurements of the kinematic Sunyaev-Zeldovich (kSZ) effects with the CMB-S4 data, the sensitivity could be improved and reach $\sigma(\tau) = 0.002$, very close to the cosmic variance limit (CVL) [30]. These values have to be compared to $\sigma_{\text{Pl}}(\tau) = 0.007$ from Planck 2018 [16]. One can then estimate how the constraints shown in Figure 3 would improve with future CMB experiments by considering the improved sensitivities on the determination of the optical depth. Here we impose $\tau < \tau_{\text{Pl}} + 2 \times \sigma_{\text{fut}}(\tau)$, i.e., assuming that the central value of τ would not change but the error would be decreased to $\sigma_{\text{fut}}(\tau) < \sigma_{\text{Pl}}(\tau)$. The resulting forecasts are shown in Figure 4. Considering $\sigma_{\text{fut}}(\tau) = 0.002$, the CMB bound assuming a FG reionization (dashed orange line) could become at least as strong as the current PUCH limit with $\sigma_{\text{Pl}}(\tau) = 0.007$. This implies that with CMB-S4 & kSZ, the bound arising from CMB anisotropies could become as good as the one from the Leo-T

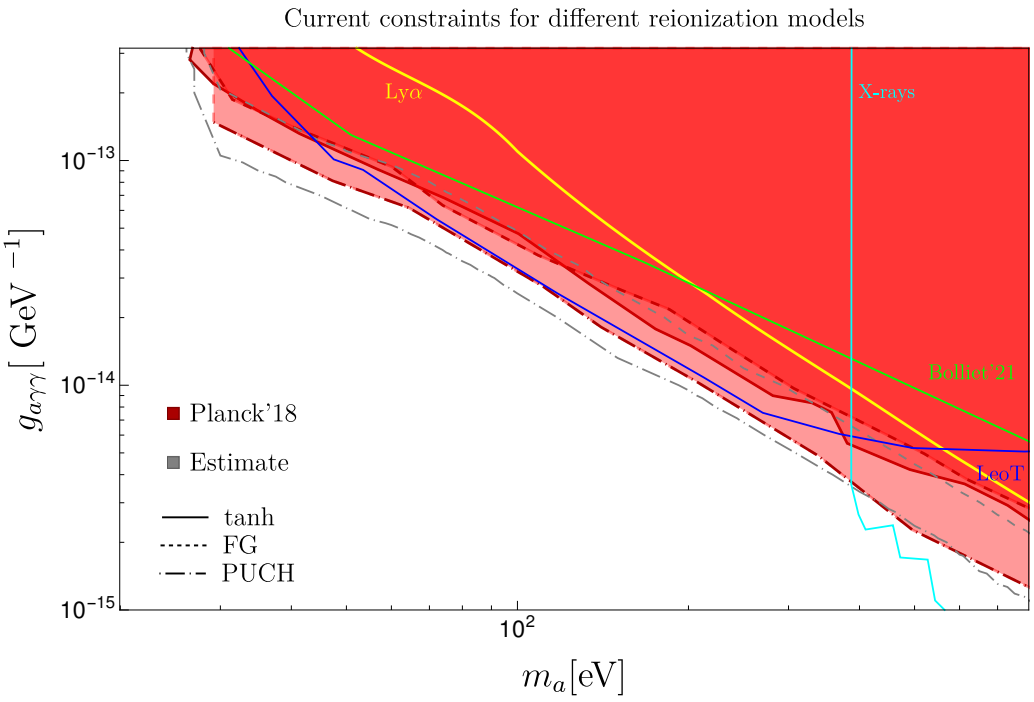

FIGURE 3: *Exclusion limits from CMB anisotropies* in the $(m_a\,[\mathrm{eV}], g_{a\gamma\gamma}[1/\mathrm{GeV}])$ plane. The red lines correspond to the regions excluded at 99% CL from Planck 2018 data for different reionization histories: the standard hyperbolic tangent description (continuous), the Fauchere-Giguère (FG) model (dashed) and the Puchwein (PUCH) model (dot-dashed). In the case of FG and PUCH models, the corresponding gray lines show a rough estimate of the exclusion limits based on the evaluation of the optical depth to reionization. The yellow continuous line represents the most stringent constraint derived in Section 4 from Lyman-α data assuming a tanh reionization. The other continuous colored lines correspond to existing limits from a previous CMB analysis [2] (green), X-ray analysis [1] (cyan) as well as the conservative constraint from Leo-T [28] (blue).

gas temperature [28], even in the more conservative reionization model considered here (FG). Very interestingly, in the case of a reionization model such as the PUCH one, basically any improvement in the precision of the optical depth to reionization will improve upon the Leo-T bound. Furthermore, we also show in Figure 4 the estimate of the limit for a modest improvement from $\sigma_{\mathrm{Pl}}(\tau) = 0.007$ to $\sigma_{\mathrm{fut}}(\tau) = 0.005$ with a dot-dashed orange line. Such a small improvement would increase the CMB bound on $g_{a\gamma\gamma}$ by almost one order of magnitude and become the most stringent bound on this mass range.

4. LYMAN-α CONSTRAINTS

In the previous section, we have used CMB anisotropies to constrain the effects of the DM energy injections on the ionization history. However, and as aforementioned, DM decays also affect the IGM temperature, see, e.g., Figure 1 (right panel). Using recent determinations of the IGM temperature in the redshift range $3.6 < z < 5.8$ from Lyman-α data [31, 32], the authors of [6] derived constraints on the mass and coupling to photons of DM particles with masses above 10 keV. They have used the `TIGM` branch of the `DarkHistory` code, where they implemented a modified chi-square test that only penalizes temperature histories that overheat the IGM compared to the data. In this section, we extend such an analysis down to DM masses of 30 eV, using our modified version of the `TIGM` branch of the `DarkHistory` code.

The analysis of [6] includes conservative assumptions concerning the astrophysical sources of heating and ionization. On the one hand, the astrophysical source for photoheating is set to zero ($\mathcal{H}_{\mathrm{X}}^{\gamma\text{-heat}} = 0$ in equation (11)) whereas a minimal astrophysical HI photoionization rate, denoted by $\Gamma_{\mathrm{HI}}^{\gamma\text{-ion}}$ in equation (11), is considered. The latter is obtained by requiring that all the contributions to the ionized fraction sum up, at small redshifts (from the onset of reionization until today) to the hyperbolic tangent model discussed in Section 2.3.1 with a z_{reio} within 1σ of the central value of Planck 2018 data. In practice, one imposes

$$\dot{x}_{\mathrm{HII}}^{\mathrm{astro}} = \frac{\dot{x}_e^{\mathrm{tanh}}}{1+\mathcal{F}_{\mathrm{He}}} - \dot{x}_{\mathrm{HII}}^{\mathrm{DM}} - \dot{x}_{\mathrm{HII}}^{(0)}, \tag{16}$$

where it has been assumed that Hydrogen and Helium have similar ionized fractions so that $x_{\mathrm{HII}}^{\mathrm{tanh}} = x_e^{\mathrm{tanh}}/(1+\mathcal{F}_{\mathrm{He}})$, with $\mathcal{F}_{\mathrm{He}} = n_{\mathrm{HeII}}/n_{\mathrm{H}}$ the ratio of singly ionized Helium to Hydrogen atoms.

We have performed a systematic analysis to find the DM parameters $(m_a, g_{a\gamma\gamma})$ that are excluded by the Lyman-α data at 95% CL due to overheating of the IGM temperature. In Figure 5, we present these bounds in terms of the DM mass and lifetime, which

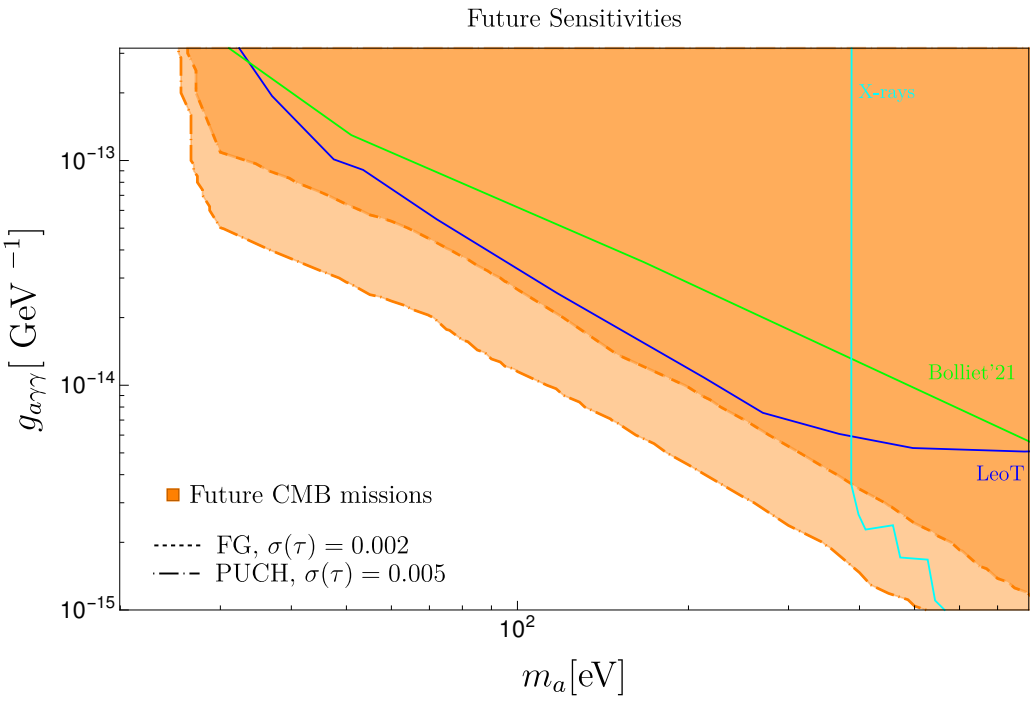

FIGURE 4: *Sensitivities of future CMB missions.* The orange lines correspond to future bounds that could be reached in the $(m_a\,[\mathrm{eV}], g_{a\gamma\gamma}[1/\mathrm{GeV}])$ plane assuming a fiducial PUCH (dot-dashed) (FG (dashed)) reionization model and a 1σ error on τ reduced to 0.005 (0.002). Other continuous colored lines correspond to existing limits from a conservative Leo-T analysis [28] (blue), a previous CMB analysis [2] (green) and X-ray limits [1] (cyan).

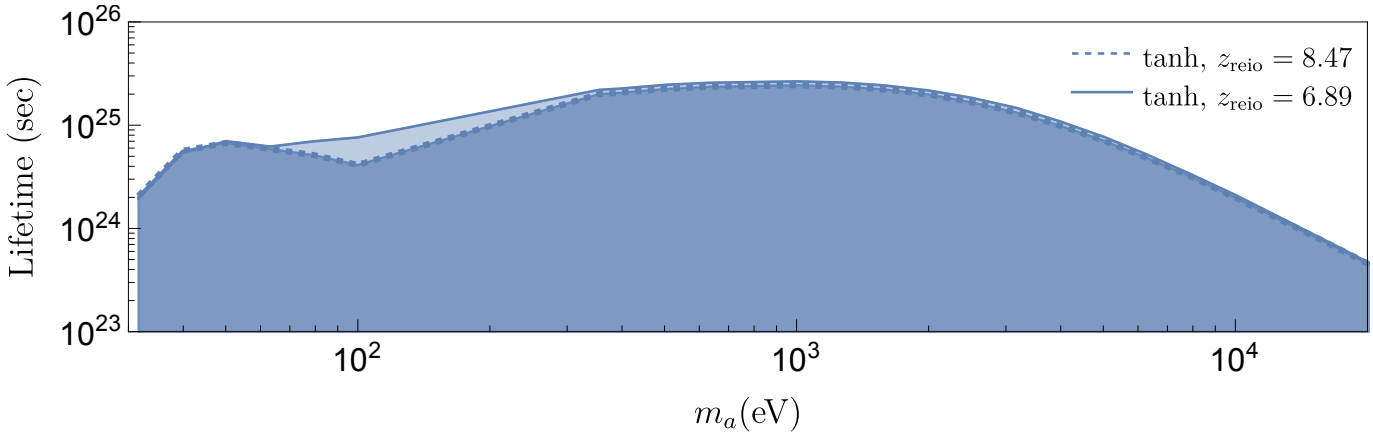

FIGURE 5: *Constraints on the lifetime of DM decay to two photons from IGM temperature data* at 95% CL assuming a tanh model for the ionized fraction. The lighter (darker) contours refers to reionization histories that start at a redshift 1σ above (below) the central value measured by Planck 2018 data.

is equal to $\Gamma_{\mathrm{dec}}^{-1}$ with Γ_{dec} given by equation (5), and their dependence on z_{reio}. In the mass range between 30 eV to 1 keV we obtain bounds on the lifetime between 2×10^{24} and 2×10^{25} seconds. The bounds are stronger for late reionizations and can differ by up to a factor of three, for masses $\sim$100 eV, between the largest and smallest z_{reio} consider in this work. This can be traced back to the small bump in temperature arising at the onset of reionization. There we see that for late reionization scenarios this small increase in temperature is probed by the Lyman-α data, while for earlier reionizations the bump happens at larger redshifts where there is no data yet. Furthermore, we find that the bump is more prominent for DM masses around 100 eV thus causing the biggest difference at those masses.

Finally, in order to compare the Lyman-α bounds obtained here to the ones from the CMB analysis derived in the previous section, we project in Figure 3, the most stringent constraint on the lifetime shown in Figure 5 (for $z_{\mathrm{reio}} = 6.89$) with a continuous yellow line. As we see, the very conservative assumption made here on the heating of the IGM in a tanh model gives rise to a bound that can readily compete with the previous CMB bounds from [2] for $m_a \gtrsim 200$ eV. They can however not compete with the most recent CMB bounds derived in Section 3.

5. CONCLUSION

We have derived new constraints on ALP decays into two photons considering the three reionization models mentioned above. For that purpose, we have modified `CLASS` to interpolate the reionization histories at low redshifts and the effective energy deposition efficiencies at higher redshifts over the DM masses and coupling to photons considered in this work. The effective energy deposition efficiencies were taken to be constant in time and equal to $f_c(x_e, z = 300)$ following the findings of [26]. We then performed an MCMC analysis including the baseline TT,TE,EE and low E Planck 2018 likelihoods and ran over a set of cosmological parameters including the DM mass and coupling to photons as well as the reionization redshift when considering a tanh model. Compared with previous works [1, 2], our analysis improves the bounds on the DM lifetime by exploiting the full CMB anisotropy spectrum information of the latest Planck data release, and explores for the first time their dependence on the astrophysical models for reionization using the self-consistent evaluation of x_e.

The summary plot of all our results is provided in Figure 3. In particular, the three red lines delimit the regions on the ALP parameter space (mass and coupling to photons) that are excluded at 99% CL for the three reionization models that we have considered. Note however that, by properly re-expressing the bounds on $g_{a\gamma\gamma}$ in terms of the DM lifetime, our constraints apply to any other DM model decaying to two photons. The limits are slightly more stringent in the case of the PUCH model [5]. This is expected as in the latter case the optical depth to reionization in the absence of DM energy injections is already significantly larger than the central value obtained with Planck 2018 and a tanh model. Overall, the CMB bounds obtained here are competitive with previous existing constraints in the mass range from 20.4 eV to 400 eV, except for the Leo-T bound from [28]. Let us emphasize though that the Leo-T and CMB bounds are independent as they rely on very different astrophysical and cosmological phenomena and assumptions. In Figure 4, we have estimated the sensitivity of future CMB surveys and concluded that the latter shall give rise to constraints competitive with the Leo-T bound, even in the most conservative reionization scenarios.

We have also analyzed the evolution of the IGM temperature. The recent advancements in hydrodynamical simulations and in the measurements of Lyman-α data have allowed a determination of the IGM temperature at redshifts $z < 7$. These data have been used in [6] to set bounds on the decay rate to photons of DM particles with masses above 10 keV. Here we have extended this analysis to lower masses taking care of accounting for the cooling from collisional excitations processes in the high redshift range, before the onset of reionization. Assuming a tanh model for the ionized fractions, our final constraints on the DM lifetime are illustrated in Figure 5 with two different reionization redshifts that correspond to the $\pm 1\sigma$ values around the central value obtained from the Planck 2018 data. The most stringent of these bounds is also reported in Figure 3 with a yellow line to ease the comparison with the CMB limits. It appears that, given the methodology followed here, the Lyman-α bounds are up to one order of magnitude weaker than the CMB bounds obtained in Section 3.

References

[1] Davide Cadamuro and Javier Redondo. Cosmological bounds on pseudo Nambu-Goldstone bosons. *JCAP*, 02:032, 2012. doi: 10.1088/1475-7516/2012/02/032.

[2] Boris Bolliet, Jens Chluba, and Richard Battye. Spectral distortion constraints on photon injection from low-mass decaying particles. *Mon. Not. Roy. Astron. Soc.*, 507(3):3148–3178, 2021. doi: 10.1093/mnras/stab1997.

[3] Hongwan Liu, Gregory W. Ridgway, and Tracy R. Slatyer. Code package for calculating modified cosmic ionization and thermal histories with dark matter and other exotic energy injections. *Phys. Rev. D*, 101(2):023530, 2020. doi: 10.1103/PhysRevD.101.023530.

[4] Claude-André Faucher-Giguère. A cosmic UV/X-ray background model update. *Mon. Not. Roy. Astron. Soc.*, 493(2):1614–1632, 2020. doi: 10.1093/mnras/staa302.

[5] Ewald Puchwein, Francesco Haardt, Martin G. Haehnelt, and Piero Madau. Consistent modelling of the meta-galactic UV background and the thermal/ionization history of the intergalactic medium. *Mon. Not. Roy. Astron. Soc.*, 485(1):47–68, 2019. doi: 10.1093/mnras/stz222.

[6] Hongwan Liu, Wenzer Qin, Gregory W. Ridgway, and Tracy R. Slatyer. Lyman-α constraints on cosmic heating from dark matter annihilation and decay. *Phys. Rev. D*, 104(4):043514, 2021. doi: 10.1103/PhysRevD.104.043514.

[7] P. J. E. Peebles. Recombination of the Primeval Plasma. *Astrophys. J.*, 153:1, 1968. doi: 10.1086/149628.

[8] Ya. B. Zeldovich and R. A. Sunyaev. The Interaction of Matter and Radiation in a Hot-Model Universe. *Astrophys. Space Sci.*, 4:301–316, 1969. doi: 10.1007/BF00661821.

[9] Tom Theuns, Anthony Leonard, George Efstathiou, F. R. Pearce, and P. A. Thomas. P**3M-SPH simulations of the lyman-alpha forest. *Mon. Not. Roy. Astron. Soc.*, 301:478–502, 1998. doi: 10.1046/j.1365-8711.1998.02040.x.

[10] James S. Bolton and Martin G. Haehnelt. The nature and evolution of the highly ionized near-zones in the absorption spectra of z˜=6 quasars. *Mon. Not. Roy. Astron. Soc.*, 374:493–514, 2007. doi: 10.1111/j.1365-2966.2006.11176.x.

[11] Tracy R. Slatyer, Nikhil Padmanabhan, and Douglas P. Finkbeiner. CMB Constraints on WIMP Annihilation: Energy Absorption During the Recombination Epoch. *Phys. Rev. D*, 80:043526, 2009. doi: 10.1103/PhysRevD.80.043526.

[12] Julien Lesgourgues. The Cosmic Linear Anisotropy Solving System (CLASS) I: Overview. 4, 2011.

[13] Diego Blas, Julien Lesgourgues, and Thomas Tram. The Cosmic Linear Anisotropy Solving System (CLASS) II: Approximation schemes. *JCAP*, 07:034, 2011. doi: 10.1088/1475-7516/2011/07/034.

[14] Julien Lesgourgues and Thomas Tram. Fast and accurate CMB computations in non-flat FLRW universes. *JCAP*, 09:032, 2014. doi: 10.1088/1475-7516/2014/09/032.

[15] Antony Lewis. Cosmological parameters from WMAP 5-year temperature maps. *Phys. Rev. D*, 78:023002, 2008. doi: 10.1103/PhysRevD.78.023002.

[16] N. Aghanim et al. Planck 2018 results. VI. Cosmological parameters. *Astron. Astrophys.*, 641:A6, 2020. doi: 10.1051/0004-6361/201833910. [Erratum: Astron.Astrophys. 652, C4 (2021)].

[17] Julien Lesgourgues. The cosmic linear anisotropy solving system (class) i: Overview, 2011. URL `https://arxiv.org/abs/1104.2932`.

[18] Patrick Stöcker, Michael Krämer, Julien Lesgourgues, and Vivian Poulin. Exotic energy injection with ExoCLASS: Application to the Higgs portal model and evaporating black holes. *JCAP*, 03:018, 2018. doi: 10.1088/1475-7516/2018/03/018.

[19] Matteo Lucca, Nils Schöneberg, Deanna C. Hooper, Julien Lesgourgues, and Jens Chluba. The synergy between CMB spectral distortions and anisotropies. *JCAP*, 02:026, 2020. doi: 10.1088/1475-7516/2020/02/026.
[20] Xue-Lei Chen and Marc Kamionkowski. Particle decays during the cosmic dark ages. *Phys. Rev.*, D70:043502, 2004. doi: 10.1103/PhysRevD.70.043502.
[21] Yacine Ali-Haimoud and Christopher M. Hirata. Ultrafast effective multi-level atom method for primordial hydrogen recombination. *Phys. Rev. D*, 82:063521, 2010. doi: 10.1103/PhysRevD.82.063521.
[22] Nanoom Lee and Yacine Ali-Haïmoud. HYREC-2: a highly accurate sub-millisecond recombination code. *Phys. Rev. D*, 102(8):083517, 2020. doi: 10.1103/PhysRevD.102.083517.
[23] Nikhil Padmanabhan and Douglas P. Finkbeiner. Detecting dark matter annihilation with CMB polarization: Signatures and experimental prospects. *Phys. Rev. D*, 72:023508, 2005. doi: 10.1103/PhysRevD.72.023508.
[24] Tracy R. Slatyer. Indirect Dark Matter Signatures in the Cosmic Dark Ages II. Ionization, Heating and Photon Production from Arbitrary Energy Injections. *Phys. Rev. D*, 93(2):023521, 2016. doi: 10.1103/PhysRevD.93.023521.
[25] Roberta Diamanti, Laura Lopez-Honorez, Olga Mena, Sergio Palomares-Ruiz, and Aaron C. Vincent. Constraining Dark Matter Late-Time Energy Injection: Decays and P-Wave Annihilations. *JCAP*, 02:017, 2014. doi: 10.1088/1475-7516/2014/02/017.
[26] Tracy R. Slatyer and Chih-Liang Wu. General Constraints on Dark Matter Decay from the Cosmic Microwave Background. *Phys. Rev. D*, 95 (2):023010, 2017. doi: 10.1103/PhysRevD.95.023010.
[27] Douglas P. Finkbeiner, Silvia Galli, Tongyan Lin, and Tracy R. Slatyer. Searching for Dark Matter in the CMB: A Compact Parameterization of Energy Injection from New Physics. *Phys. Rev. D*, 85:043522, 2012. doi: 10.1103/PhysRevD.85.043522.
[28] Digvijay Wadekar and Zihui Wang. Strong constraints on decay and annihilation of dark matter from heating of gas-rich dwarf galaxies. *Phys. Rev. D*, 106(7):075007, 2022. doi: 10.1103/PhysRevD.106.075007.
[29] Thejs Brinckmann and Julien Lesgourgues. MontePython 3: boosted MCMC sampler and other features. *Phys. Dark Univ.*, 24:100260, 2019. doi: 10.1016/j.dark.2018.100260.
[30] Kevork Abazajian et al. CMB-S4 Science Case, Reference Design, and Project Plan. 7, 2019.
[31] Michael Walther, Jose Oñorbe, Joseph F. Hennawi, and Zarija Lukić. New Constraints on IGM Thermal Evolution from the Lyα Forest Power Spectrum. *Astrophys. J.*, 872(1):13, 2019. doi: 10.3847/1538-4357/aafad1.
[32] Prakash Gaikwad et al. Probing the thermal state of the intergalactic medium at $z > 5$ with the transmission spikes in high-resolution Ly α forest spectra. *Mon. Not. Roy. Astron. Soc.*, 494(4):5091–5109, 2020. doi: 10.1093/mnras/staa907.